On the agglomeration and breakage of particles in turbulent flows through pipe bends using CFD-PBE

Bilde, Kasper Gram; Hærvig, Jakob; Lehnigk, Ronald; Schlegel, Fabian; Sørensen, Kim

Published in:
Chemical Engineering Science

DOI (link to publication from Publisher):
10.1016/j.ces.2022.117915

Publication date:
2022

Document Version
Publisher's PDF, also known as Version of record

Chemical Engineering Science 260 (2022) 117915

Contents lists available at ScienceDirect

Chemical Engineering Science

journal homepage: www.elsevier.com/locate/ces

On the agglomeration and breakage of particles in turbulent flows through pipe bends using CFD-PBE

Kasper Gram Bilde [a,b,*], Jakob Hærvig [a], Ronald Lehnigk [c], Fabian Schlegel [c], Kim Sørensen [a]

[a] Aalborg University, AAU Energy, Pontoppidansstræde 111, Aalborg 9220, Denmark
[b] Alfa Laval Aalborg A/S, Gasværksvej 21, Aalborg 9000, Denmark
[c] Helmholz Zentrum Dresden Rossendorf, Institute of Fluid Dynamics, Bautzner Landstraße 400, Dresden 01328, Germany

HIGHLIGHTS

- The effect of bend radius on the particle size becomes negligible when Re_f > 30,000.
- Lower Reynolds numbers and larger bend radius result in larger particles.
- The particle size distribution of flocculated soot is replicated using CFD-PBE.
- Periodic boundary conditions are applied to obtain a steady-state solution.

GRAPHICAL ABSTRACT

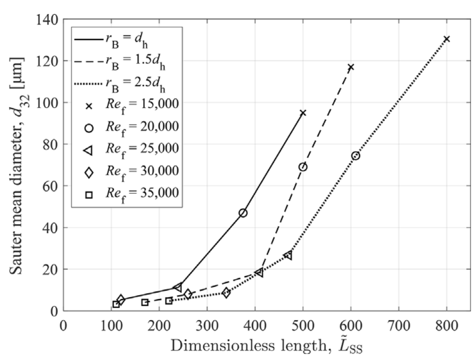

ARTICLE INFO

Article history:
Received 22 February 2022
Received in revised form 17 May 2022
Accepted 13 July 2022
Available online 19 July 2022

Keywords:
Multiphase flows
Population balance equation
Population balance modelling
CFD-PBE
Agglomeration and breakage
Turbulence
Flocculation

ABSTRACT

Predicting the agglomeration and breakage of solid particles is important when designing a compact and efficient water purification process. A coupled computational fluid dynamics model is presented where the population balance equation is applied to track the particle size distribution for a periodic turbulent pipe flow with 180° bends for fluid Reynolds numbers of $15,000 < Re_f < 35,000$ and pipe bend radii of $r_B = d_h, r_B = 1.5d_h$ and $r_B = 2.5d_h$. The critical parameters in the Euler-Euler model are analysed and values are chosen to describe the agglomeration of soot particles based on an experimentally obtained particle size distribution measured using a Malvern Mastersizer 3000. It is concluded that the particle Sauter mean diameter converges to a constant value independent of the pipe bend radius when $Re_f > 30,000$. The Sauter mean diameter increases from $d_{32} = 42.7\,\mu m$ to $d_{32} = 95\,\mu m$ without changing the total length of the static flocculator by choosing $r_B = d_h$ and $Re_f = 15,000$.

1. Introduction

The aggregation and breakage of particles in turbulent flows are relevant to a wide range of industries and applications, involving several topics in the chemical sector. In both the wastewater- and clean water industry, the aggregation and breakage of solid particles are commonly a problem which is investigated and analysed using both experimental and numerical techniques. Examples of industrial applications are the formation of powders (Tong et al., 2016), production of pharmaceuticals (Palzer, 2011), the formation of soot during combustion (Bhandari et al., 2019) and in flocculation systems for water purification purposes (Lee et al., 2014). In

* Corresponding author at: Aalborg University, AAU Energy, Pontoppidansstræde 111, Aalborg 9220, Denmark.
E-mail address: kgb@energy.aau.dk (K.G. Bilde).

https://doi.org/10.1016/j.ces.2022.117915
0009-2509/

this paper, we focus on water purification where the scope of the study is to analyse the particle size distribution for different geometrical configurations and fluid Reynolds numbers.

In wastewater treatment plants solid particles are agglomerated in a stirred reactor or by in-line mixers to reduce sedimentation time (Bratby, 2006). Several researchers have, since the 1970s, carried out experimental studies on particle aggregation systems (Vrale and Jorden, 1971, 1972, 1991, 1994, 2001, 2004, 2016, 2018). In more recent years, computational fluid dynamics (CFD) has been extensively applied to improve the understanding of applications that are used to agglomerate particles. Traditionally, the performance of wastewater pretreatment systems has been characterised by the velocity gradient and energy dissipation rate, as proposed by Camp and Stein (1943). As these parameters are directly available using CFD, this approach is highly advantageous.

Ducoste and Clark (1999) were among the first to apply CFD to describe particle aggregation in flocculation systems. The authors used the CFD code FIDAP to evaluate the fluid mechanics in a flocculator using the standard k-ε turbulence model. The numerical results were compared to experimental results using laser Doppler velocimetry. However, the CFD code applied by the researchers did not produce accurate results for the energy dissipation for the swirling flow in the reactor.

Bridgeman et al. (2010) highlighted the applicability of CFD in the development of particle aggregation systems for wastewater treatment plants. They analysed the difference and impact of several turbulence models within the Reynolds averaged Navier Stokes (RANS) framework. The authors were successful in highlighting zones in the system where high-velocity gradients were present, causing particles to break up. Historically, flocculation systems have been designed from a global perspective using either the total pressure loss or the power input to the mechanical actuator (Vrale and Jorden, 1971; Mhaisalkar et al., 1991) but Bridgeman et al. (2010) proposed that a local design perspective using CFD improves the overall performance of the application.

To simulate the aggregation and breakage of discrete particles in a continuous flow, several different multiphase methods have been used. A widely applied approach is to couple CFD and the discrete element model (DEM), where discrete particles are tracked using a Lagrangian soft-sphere model. Hærvig et al. (2018) analysed particle deposition and aggregation in straight turbulent pipe flows with a large eddy simulation (LES) in order to adequately describe the turbulence in the continuous phase. A periodic boundary condition was applied to the pipe section, thereby effectively resulting in an infinitely long straight circular pipe. The CFD-DEM model successfully described the aggregation and breakage of dilute particles in a turbulent gas using the surface adhesion theory proposed by Johnson et al. (1971). Dizaji et al. (2019) analysed the collision and breakage of loosely coupled agglomerates in a shear flow using a four-way coupled CFD-DEM approach. The authors demonstrated in high detail, how agglomerates break into several fragments when placed in a shear flow. Furthermore, they showed how two agglomerates can merge into a single agglomerate, bounce off each other, or fragment into several new smaller agglomerates during a collision. The details of the modelling framework for both the particle and fluid phase are extensive, thereby producing accurate results but at a high computational cost.

Due to the high computational demand of the Euler–Lagrangian CFD-DEM approach, alternative methods have been proposed, which are computationally less demanding. They involve an approximate solution of the population balance equation (PBE), which tracks the temporal and spatial evolution of the particle number density function. Several methods have been proposed to solve the PBE, including the least-square spectral element method (Zhu et al., 2009), the finite element method (Ganesan, 2012) and the family of various method of moments (MOM). One of the most widely used approaches is the quadrature method of moments (QMOM), first implemented into the commercial CFD code Fluent by Marchisio et al. (2003) for modelling simultaneous aggregation and breakage of particles. The QMOM solves for a consecutive set of lower-order integer moments of the number density function and utilises Gaussian quadrature for approximating the integral source terms of the PBE. The QMOM was extended by Yuan et al. (2012) to solve the continuous number density function in the Extended QMOM (EQMOM) approach. Passalacqua et al. (2018) implemented the EQMOM into the OpenFOAM CFD library under the OpenQBMM module. The authors successfully described the aggregation of dilute particles in a Taylor-Couette flow reactor.

Another approach to solving the PBE is the class method, alternatively referred to as the sectional or discrete method. Using this approach, the number density function is discretised into a range of size classes, resulting in a set of source term coupled transport equations for individual number concentrations. The integral source terms are transformed into summations over subintervals. Lehnigk et al. (2021) successfully implemented the class method of Kumar and Ramkrishna (1996) into the Euler-Euler model, also referred to as the two-fluid model, of OpenFOAM. They applied it to simulate both the co-current flow of air and water in a vertical pipe as well as the synthesis of titania in a tubular furnace reactor.

The advantage of the QMOM is that it requires a low number of transported scalars to account for statistical moments which makes this method computationally advantageous. This modelling approach, however, does not provide direct information about the number density function, meaning its shape is unknown. It can be obtained with the EQMOM, as it approximates the number density function through a combination of kernel density functions. However, Li et al. (2017) report that the EQMOM can be up to 30 times as computationally demanding as the QMOM, resulting from costly source term calculations. Class methods are costly as well and require a priori knowlegde of the size range, but the number density function is readily available at any point in the computational domain.

In this study, the PBE is solved using the class method implementation of Lehnigk et al. (2021), as the scope of this study is to analyse the impact on the shape of the number density function when altering the geometrical configuration and the fluid Reynolds number. Furthermore, the class method allows for a direct comparison with experimental data, as the size distribution is directly available. The aggregation and breakage of solid particles throughout circular pipe U-bends are modelled and analysed for fluid Reynolds numbers ranging from $15,000 < Re_{\mathrm{f}} < 35,000$ using the Euler-Euler model of OpenFOAM. Special care is taken to model the aggregation, breakage and external force acting on the solid particles and agglomerates suspended in the flow. The numerical results are compared to an experimentally obtained particle size distribution for an in-line flocculator designed to agglomerate soot particles.

2. Experimental setup

A particle size distribution of agglomerated soot particles was measured and presented in this study for the process seen in Fig. 1. A 2 MW engine (MAN 9L28/32H) is operated on heavy fuel oil with a sulphur content of 2.5% w/w. As the fuel contains a high sulphur content, a wet scrubber is used to remove the sulphur content from the exhaust gas by scrubbing the exhaust gas with a water film inside the wet scrubber. As a bi-product, up to 40% of the particulate mass in the exhaust gas is trapped by the water film and transferred from the gas phase to the water phase (Simonsen, 2018). The trapped particulate mass in the wet scrubber is

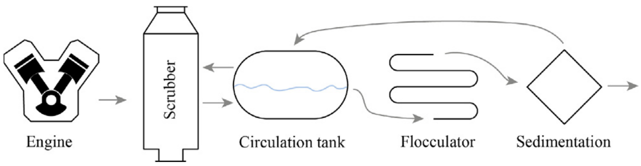

Fig. 1. Process overview of the system that produces the soot that is agglomerated in the flocculator. Flue gas from a 2 MW engine is cleaned using a wet scrubber, where the soot is trapped in the wet scrubber by a water film. The dirty water is recirculated over the scrubber and through a water purification application. The soot particles are agglomerated in a static flocculator, which is where the particle size distribution is measured.

primarily soot and black carbon, which is formed within the cylinder of the engine during combustion, and a percentage of residual lube oil. In this study, the particulate mass is assumed as a single component, namely as soot. The water is recirculated over the wet scrubber through a circulation tank and continuously cleaned in a water purification system through fast sedimentation using a high-speed centrifugal separator. The clean water is recirculated back to the circulation tank and the particles are removed from the system as a sludge. To achieve a shorter sedimentation time, the suspended soot particles are agglomerated using an in-line static flocculator consisting of 11x straight pipes followed by 180° pipe bends, which is also seen in Fig. 2. By producing larger agglomerates over the static flocculator, the water purification process becomes more effective, as a shorter sedimentation time is needed. Aluminium chloride (Kemira PAX-18) is dosed as a metal coagulant at the inlet of the static flocculator to reduce the net surface charge of the soot particles. Further, a highly cationic polymer flocculant (BASF Zetag 9048FS) is dosed into the process stream, in a Venturi-like static mixer after a total of 4x 180° pipe bends, to strengthen and further agglomerate the particles. The net surface charge of the particles is reduced as the soot particles are negatively charged and this makes the particles stable within the suspension.

The static flocculator, shown in more detail in Fig. 2, features a pipe bend radius of $r_B = 1.5d_h$ and is operated at a fluid Reynolds number of $Re_f = 22,500$, which corresponds to a fluid bulk velocity of $\bar{u}_f = 0.563\,\mathrm{m/s}$. The particle size distribution of the agglomerated soot is measured for the wet scrubber re-circulation water prior to sedimentation in the water purification application. Agglomerated soot particles are extracted at the outlet of the static flocculator and the particle size distribution is analysed using a Malvern Mastersizer 3000, which uses the technique of laser diffraction to measure the particle size distribution. The total suspended solid concentration is measured using EN 872:2005 to determine the particle mass concentration. The volumetric concentration is then estimated using the assumption that soot primarily consists of graphite layers, (Wang et al., 2018), with a density of $\rho_p = 1400\ \mathrm{kg/m^3}$ yielding a bulk volumetric concentration of $\alpha_p = 0.1\%$.

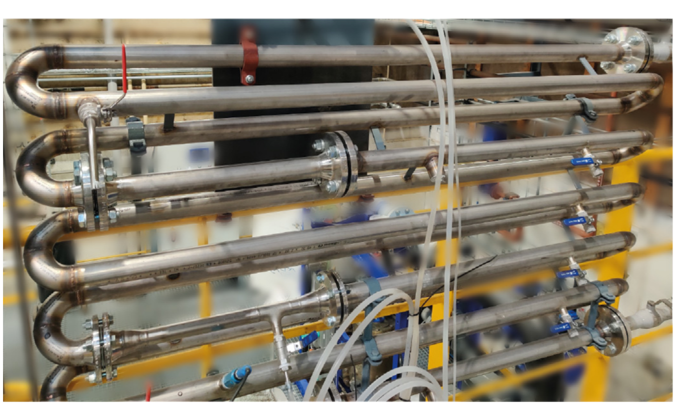

Fig. 2. In-line pre-treatment static flocculator. The flocculator consists of a set of 180° pipe bends and a metal coagulant is dosed at the inlet of the application and the dosing of the cationic polymer is performed after a total of 4x 180° pipe bends. The particle size distribution is measured at the outlet of the static flocculator.

3. Numerical framework

The simulations are carried out with the mesh shown in Fig. 3. The computational domain is designed to use periodic boundary conditions, i.e. the outgoing velocity profile, turbulence characteristics and particle properties are reapplied at the inlet. This effectively results in an infinite number of U-bends followed by a straight section with a length of $L = 20d_h$, which allows a steady-state solution to be obtained. Pipe bend radii of $r_B = d_h, r_B = 1.5d_h$ and $r_B = 2.5d_h$ are analysed in this study, as those are commonly used in industrial applications.

The Euler-Euler model is applied to simulate the fluid and particle flow. In the following sections, the governing equations for the fluid and particle phases as well as the particle–particle interaction are presented.

3.1. Governing equations for multiphase flow

In the Euler-Euler model, a separate set of equations for continuity and momentum is solved for each phase φ as seen in Eq. (1) and (2), respectively.

$$\frac{\partial}{\partial t}\left(\alpha_\varphi \rho_\varphi\right) + \nabla \cdot \left(\alpha_\varphi \rho_\varphi \boldsymbol{u}_\varphi\right) = 0 \tag{1}$$

$$\frac{\partial}{\partial t}\left(\alpha_\varphi \rho_\varphi \boldsymbol{u}_\varphi\right) + \nabla \cdot \left(\alpha_\varphi \rho_\varphi \boldsymbol{u}_\varphi \boldsymbol{u}_\varphi\right) - \nabla \cdot \tau_\varphi = -\alpha_\varphi \nabla p + \alpha_\varphi \rho_\varphi \boldsymbol{g} + \boldsymbol{M}_\varphi + \boldsymbol{S}_\varphi, \tag{2}$$

where α is the volumetric fraction, ρ the density, $\boldsymbol{u}$ the velocity, $\boldsymbol{S}$ represents the momentum source due to volume forces, $\boldsymbol{g}$ the gravitational acceleration, p the pressure, $\boldsymbol{\tau}$ the stress tensor, which also includes the Reynolds stresses for the fluid phase and $\boldsymbol{M}_\varphi$ is the rate of interfacial momentum transfer between the phases which is given by

$$\boldsymbol{M}_\varphi = \sum_{\varphi=0,\varphi\neq\psi}^{N} \left(\boldsymbol{F}_{\mathrm{D},\varphi\psi} + \boldsymbol{F}_{\mathrm{L},\varphi\psi} + \boldsymbol{F}_{\mathrm{VM},\varphi\psi} + \boldsymbol{F}_{\mathrm{disp},\varphi\psi}\right), \tag{3}$$

where the subscripts denotes drag force, D, lift force, L, virtual mass force, VM, and turbulent dispersion force, disp, between phase φ and ψ. Conservation of momentum implies that $\sum_\varphi \boldsymbol{M}_\varphi = 0$. It is assumed that the pressure is shared between the phases. A momentum source term $\boldsymbol{S}_\varphi$ is applied for the fluid phase in this study to balance the pressure gradient in the periodic domain, which acts to ensure a mean bulk velocity corresponding to the fluid Reynolds number chosen. To this end, a pressure gradient increment is added to the existing pressure gradient of the fluid phase for each iteration, based on the difference between the fluid velocity and the desired bulk velocity at the given time step.

3.1.1. Turbulence modelling

Several authors have applied the re-normalisation group turbulence model (RNG) by Yakhot and Orszag (1986), to successfully describe the turbulence in swirling flows, such as flow through a pipe bend or fluid separation flows (Hilgenstock and Ernst, 1996; Kim et al., 2014; Cai et al., 2019; Marshall and Bakker, 2004). Kim et al. (2014) analysed the accuracy of several turbulence mod-

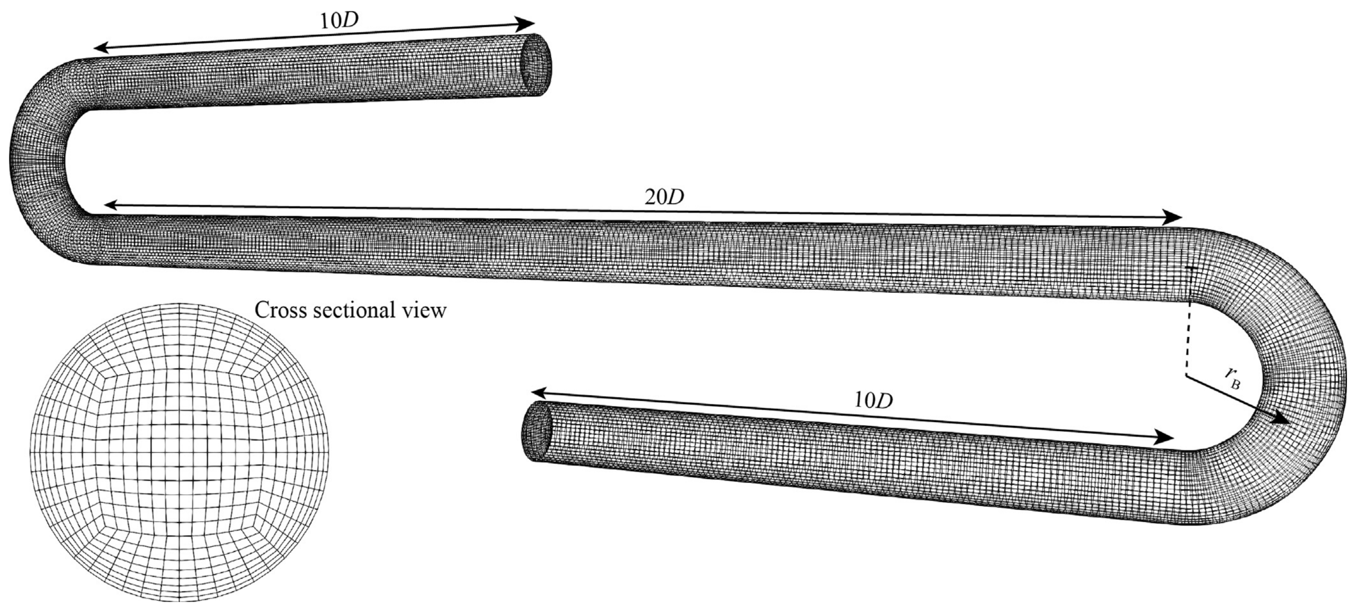

Fig. 3. Geometrical setup for the computational domain. The domain is periodic, effectively resulting in an infinite number of 180° bends followed by a straight pipe section with lengths of $L = 20d_h$. In this figure $r_B = 1.5d_h$. The mesh resolution of the cross-sectional view is also seen in the figure.

els for a 90° pipe bend including the standard k-ε, realizable k-ε, RNG-k-ε, k-ω SST model. The authors concluded that the RNG k-ε model yields good agreement for the primary stream-wise velocity and secondary swirling velocity profile compared to the other turbulence models.

Escue and Cui (2010) compared the accuracy of the RNG k-ε to the Reynolds stress model (RSM) which generally has a better prediction of turbulence, but is also more computationally expensive. The authors concluded that the results obtained by the RNG k-ε model were in better agreement with experimental data compared to the RSM for low swirling flows. Since the swirling flow is produced by a pipe bend, it is assumed that the RNG k-ε produces suitable turbulence results for this study.

The two-equation RNG k-ε model is developed by applying statistical methods used in re-normalisation group theory to resolve the smallest eddies in the inertial range. The RNG procedure removes the small scales of motion by expressing their effects in terms of larger-scale motion and modifying the turbulent viscosity. The governing equations for the RNG k-ε model by Yakhot et al. (1992) are

$$\frac{\partial}{\partial t}(\alpha_f \rho_f k) + \nabla \cdot (\alpha_f \rho_f k \boldsymbol{u}_f) = \nabla\left[\left(\mu_f + \frac{\mu_t}{\sigma_k}\right)\nabla k\right] + P_k - \alpha_f \rho_f \varepsilon \tag{4}$$

and

$$\frac{\partial}{\partial t}(\alpha_f \rho \varepsilon) + \nabla \cdot (\alpha_f \rho_f \varepsilon \boldsymbol{u}_f) = \nabla\left[\left(\mu_f + \frac{\mu_t}{\sigma_\varepsilon}\right)\nabla \varepsilon\right] + C_{1\varepsilon}\frac{\varepsilon}{k}P_k - C_{2\varepsilon}\alpha_f \rho \frac{\varepsilon^2}{k}, \tag{5}$$

where the subscript f denotes the fluid phase and P_k the generation of turbulence due to the mean velocity gradients. The model coefficients chosen for the RNG k-ε model used in this work are the default values.

3.1.2. Kinetic theory of granular flows

The stress tensor for the dispersed particle phase, $\boldsymbol{\tau}_p$, is modelled using the kinetic theory of granular flows to account for the particle–particle interactions (Lun et al., 1984; van Wachem, 2000; Yao et al., 2015; Shekhawat et al., 2018). An extensive description of the KTGF model and a comparison of the submodels included is presented by van Wachem (2000). The submodels selected here are listed in Table 1 and the corresponding mathematical expressions can be found in Appendix A.

Table 1
Submodels applied for the KTGF.

Description	Author
Conductivity of granular energy	Hrenya and Sinclair (1997)
Frictional stress	Johnson and Jackson (1987)
Generation and dissipation of granular energy	Lun et al. (1984)
Particle shear viscosity	Hrenya and Sinclair (1997)
Particle phase pressure	Lun et al. (1984)
Radial distribution function	Lun and Savage (1986)

3.2. Interfacial momentum transfer models

The rate of interfacial momentum transfer can be divided into several submodels accounting for the different fluid forces acting on the particles. The interfacial forces are defined by the drift velocity between the two phases, $\boldsymbol{u}_r = |\boldsymbol{u}_p - \boldsymbol{u}_f|$ or the particle Reynolds number, $\mathrm{Re}_p = \boldsymbol{u}_r d_p / \nu_f$.

3.2.1. Drag force

The drag force acting on the particles is described by Eq. (6)

$$\boldsymbol{F}_D = \frac{1}{2}\rho_f |\boldsymbol{u}_r| \boldsymbol{u}_r C_D A_p, \tag{6}$$

where C_D is the drag coefficient and A_p is the projected surface area of the particles as seen by the fluid. The particles are assumed spherical and the drag force coefficient presented by Wen and Yu (1966) is used in this study which reads

$$C_D = \begin{cases} \frac{24}{Re_p}\alpha_f^{-2.65} & \text{for } Re_p < 0.5 \\ \frac{24}{Re_p}\left(1 + 0.15 Re_p^{0.687}\right)\alpha_f^{-2.65} & \text{for } 0.5 \leqslant Re_p < 1000 \\ 0.44\alpha_f^{-2.65} & \text{for } Re_p \geqslant 1000. \end{cases} \tag{7}$$

Assuming the soot particles and agglomerates to be spherical is, of course, a simplification, as these are fractal-like in their nature. According to the observations of Mikhailov et al. (2006) and Ma et al. (2013) soot structures tend to collapse when entering a wet environment and thereby become quite spherical. Furthermore, as the particles are small, so is the Stokes number. For the largest particles it evaluates to $\mathrm{St} < 0.2$ and for the majority $\mathrm{St} \ll 1$, meaning that the relative velocity between the phases is small. The particles largely follow the flow and the effect of assuming sphericity is negligible.

3.2.2. Lift force

The dispersed particles are affected by shear and rotational forces in this study. The lift force acting on a dispersed phase by a continuous phase can be described as

$$\boldsymbol{F}_{\mathrm{L}} = -C_{\mathrm{L}}\rho_{\mathrm{f}}\alpha_{\mathrm{p}}\boldsymbol{u}_{\mathrm{r}} \cdot \omega, \tag{8}$$

where C_{L} is the lift force coefficient and ω is the vorticity defined by the curl operator as $\omega = \nabla \times \boldsymbol{u}_{\mathrm{f}}$. The lift force coefficient by Saffman (1965) describes the lift force coefficient for low Reynolds numbers as

$$C_{\mathrm{L}} = \frac{3}{2\pi\sqrt{Re_{\omega}}}C'_{\mathrm{L}} \tag{9}$$

where $C'_{\mathrm{L}} = 6.46$ and the vorticity Reynolds number is given as $Re_{\omega} = |\omega|d_{\mathrm{p}}^2/\nu_{\mathrm{f}}$. Mei (1992) extended the lift force coefficient to cover finite Reynolds numbers and extended the applicable range. The lift force coefficient, C'_{L}, is given as

$$C'_{\mathrm{L}} = \begin{cases} 6.46\left[(1-0.3314\beta^{0.5})e^{-0.1Re_{\mathrm{p}}} + 0.3314\beta^{0.5}\right] & Re_{\mathrm{p}} \leqslant 40 \\ 6.46 \cdot 0.0524\sqrt{\beta Re_{\mathrm{p}}} & Re_{\mathrm{p}} > 40, \end{cases} \tag{10}$$

where $\beta = 0.5(Re_{\omega}/Re_{\mathrm{p}})$.

3.2.3. Virtual mass force

The virtual mass force describing the additional mass of the fluid being accelerated along with the particulate mass is seen in Eq. (11).

$$\boldsymbol{F}_{\mathrm{VM}} = -C_{\mathrm{VM}}\rho_{\mathrm{f}}\alpha_{\mathrm{p}}\left(\frac{D_{\mathrm{p}}}{Dt}\boldsymbol{u}_{\mathrm{p}} - \frac{D_{\mathrm{f}}}{Dt}\boldsymbol{u}_{\mathrm{f}}\right), \tag{11}$$

where C_{VM} is the virtual mass force coefficient, and for this study, a constant value of $C_{\mathrm{VM}} = 0.5$ is applied. The term D_{p}/Dt and D_{f}/Dt denotes the material derivative for the particle and fluid phase respectively.

3.2.4. Turbulent dispersion force

The turbulence in the continuous phase, described by the turbulent diffusion term, is based on the averaged velocity field when using the RANS methodology. This means that the turbulent eddies in the continuous phase do not directly impact the dispersed phase as the eddies are modelled and not resolved. To account for the turbulent dispersion of the dispersed phase, Burns et al. (2004) performed a Favre averaging of the drag force. The turbulent dispersion force is given as

$$\boldsymbol{F}_{\mathrm{disp}} = -\frac{3}{4}C_{\mathrm{D}}\frac{\alpha_{\mathrm{p}}\rho_{\mathrm{f}}}{d_{\mathrm{p}}}\boldsymbol{u}_{\mathrm{r}}\frac{\nu_{\mathrm{t}}}{\sigma}\left(\frac{\nabla\alpha_{\mathrm{f}}}{\alpha_{\mathrm{f}}} - \frac{\nabla\alpha_{\mathrm{p}}}{\alpha_{\mathrm{p}}}\right), \tag{12}$$

where σ is the turbulent Schmidt number, which is set to a value of $\sigma = 0.9$ in this study.

3.3. Population balance equation

The evolution of the particle size distribution is described using the population balance equation, a transport equation for the number density function, $n(\xi, \mathbf{x}, t)$, where ξ is the internal coordinate and $\mathbf{x}$ is the spatial coordinate. In this study, the particle size distribution is of interest, which is why the internal coordinate is the volume of the particles, $\xi = v_p$. For ease of notation and since all terms depend on the spatial dimension and time, the number density function is denoted by n_v. The population balance equation is given as

$$\frac{\partial}{\partial t}n_v + \nabla \cdot (\boldsymbol{u}n_v) = S_v, \tag{13}$$

where S_v is the source term accounting for the discontinuous changes in the number density function such as aggregation and breakage, given by

$$S_v = \tfrac{1}{2}\int_0^v n_{v'}n_{v-v'}a_{v',v-v'}\,\mathrm{d}v' - n_v\int_0^\infty n_{v'}a_{v,v'}\,\mathrm{d}v' + \int_v^\infty n_{v'}b_{v'}\beta_{v,v'}\,\mathrm{d}v' - n_v b_v. \tag{14}$$

The birth and death by aggregation are given by the first two terms on the right-hand side and $a_{v,v'}$ denotes the corresponding aggregation frequency. Birth and death by breakage are described by the third and fourth term on the right-hand side of Eq. (14), where $b_{v'}$ denotes the corresponding breakage frequency. During breakage, information about the number and distribution of daughter particles is given by the daughter size distribution function, $\beta_{v,v'}$, which must satisfy the constraints

$$\int_0^{v'} v\beta_{v,v'}\,\mathrm{d}v = v', \tag{15}$$

and

$$\int_0^{v'} \beta_{v,v'}\,\mathrm{d}v = n_\beta, \tag{16}$$

where n_β is the total number of daughter particles born from particle breakage. The daughter size distribution function for this study is presented in Section 3.3.3.

Eq. (13) is solved by discretising the particle size domain into a set of size classes with an upper and lower boundaries, v_i and v_{i+1}, respectively. The number concentration, N, is given by integrating over the resulting size class

$$N_i = \int_{v_i}^{v_{i+1}} n_v\,\mathrm{d}v. \tag{17}$$

The discretised version of Eq. (13) using Eq. (17) yields

$$\frac{\partial N_i}{\partial t} + \nabla \cdot (\mathbf{u}N_i) = S_i. \tag{18}$$

The source term in Eq. (18) is obtained using the formulation proposed by Kumar and Ramkrishna (1996), where it is assumed that the population is concentrated at pivotal volumes and the mean value theorem is applied for computing the frequencies. A separate transport equation is solved for each size class. The volume concentration of the particle phase is then given as:

$$\alpha_{\mathrm{p}} = \sum_{i=0}^{k} x_i N_i\,, \tag{19}$$

where x_i is the pivotal volumes of the size class. For further details of the algorithm, the reader is referred to the work of Lehnigk et al. (2021).

3.3.1. Aggregation kernel

The birth and death of new particles due to aggregation are based on an aggregation kernel describing the aggregation frequency. In this work, the aggregation kernel proposed by Adachi et al. (1994) is adopted. It has been applied successfully by Marchisio et al. (2003) and Cai et al. (2019) to describe the aggregation of particles in turbulent flows. The aggregation frequency model is

$$a_{d,d'} = \frac{4}{3}\sqrt{\frac{3\pi}{10}}\sqrt{\frac{\varepsilon_f}{\nu_f}}(d+d')^3, \tag{20}$$

where ε_f is the turbulent dissipation rate of the continuous phase and ν_f is the kinematic viscosity of the continuous phase.

3.3.2. Breakage kernel

The birth and death of particles due to breakage are described by the breakage kernel. Here, the model proposed by Kusters (1991) is adopted. The breakage frequency model is an exponential kernel given by

$$b_{\upsilon'} = \sqrt{\frac{4}{15\pi}}\sqrt{\frac{\varepsilon}{\nu_f}}\exp\left(-\frac{\varepsilon_{cr}}{\varepsilon}\right), \tag{21}$$

where ε_{cr} is the critical rate of energy dissipation required for the agglomerate to break up. The critical rate of energy dissipation is defined as

$$\varepsilon_{cr} = \frac{B}{r_c}, \tag{22}$$

where B is a strength parameter that accounts for the critical shear velocity needed to break an agglomerate and r_c is the collision radius, which is based on a correlation proposed by Mandelbrot (1985):

$$r_c = r_0\left(\frac{n_i}{k_c}\right)^{1/D_f}. \tag{23}$$

Herein, r_0 is the radius of the primary particle in the agglomerate, n_i is the number of primary particles in the agglomerate, k_c is a constant relative to the packing density which is generally assumed to be unity (Jeldres et al., 2017) and D_f is the fractal dimension. The number of primary particles, n_i, is given by Eq. (24), where r_i is the radius of the agglomerate.

$$n_i = \left(\frac{r_i}{r_0}\right)^{D_f}. \tag{24}$$

The critical strength of the agglomerate is thereby a function of the fractal dimension and the number of primary particles in the agglomerate, meaning larger agglomerates are more likely to break compared to smaller agglomerates.

3.3.3. Daughter size distribution

A size distribution model is needed when an agglomerate breaks into smaller fragments (daughters particles). For this study a beta distribution function is chosen for the newly formed particles. Laakkonen et al. (2007) proposed a beta distribution that is a function of the number of daughter particles and is given as

$$\beta_{\upsilon,\upsilon'} = (1+C_4)(2+C_4)(3+C_4)(4+C_4)\left(\tfrac{1}{3}\right)\left(\tfrac{1}{\upsilon'}\right)\left(\tfrac{\upsilon}{\upsilon'}\right)^2\left(1-\tfrac{\upsilon}{\upsilon'}\right)^{C_4}, \tag{25}$$

where υ is the volume of the daughter particle and υ' is the volume of the mother particle. The total number of daughters generated is a function of the coefficient, C_4:

$$n_i = \frac{4}{3}+\frac{C_4}{3}. \tag{26}$$

4. Results and Discussion

4.1. Simulation parameters

The particle properties used for the simulations are seen in Table 2. The primary particle size of the agglomerates is chosen based on the measurements of Trivanovic et al. (2019) and the fractal dimension selected according to the measurements of Mikhailov et al. (2006) and Ma et al. (2013). The particle size range is discretised into 50 size classes that are distributed equally on the logarithmic scale in the range of $1\mu m < d_p < 1000\mu m$ as

Table 2
Particle properties applied for the simulations.

Property	Symbol	Value	Unit
Density	ρ_p	1400	kg/m^3
Primary particle size	d_0	250	nm
Fractal dimension	D_f	2.4	-
Coefficient of restitution	e	0.75	-

$$\log_{10}\left(\frac{d_{p,i}}{d_{p,i-1}}\right) = \frac{\log_{10}\left(\frac{d_{p,N}}{d_{p,1}}\right)}{N-1} \qquad 1 < i < N. \tag{27}$$

To ensure computational stability the Courant–Friedrichs– Lewy (CFL) condition, which determines the maximum allowed time step by considering the mesh size, is set to a maximum value of $CFL = |\boldsymbol{u}_f|\Delta t/\Delta x < 1$. The simulations were continued until a steady-state solution was obtained, which was found to be dependent on the fluid Reynolds number and the geometrical setup for the specific case. Dependent on the case, a steady-state solution was obtained after a dimensionless flow length of $300 < \tilde{L} < 1000$, where $\tilde{L} = t\cdot\bar{u}_f/d_h$ and $\bar{u}_f$ is the mean bulk velocity of the fluid. Common for all geometrical cases was that the steady-state solution was obtained faster with increasing fluid Reynolds number.

The experiment features a total dimensionless length of $\tilde{L} = 500$. A length of $\tilde{L} = 350$ is experienced by the fluid after the polymer flocculant is dosed into the process stream. In the simulation, the particulate phase is inserted into a fully developed flow field and then the dimensionless flow length needed to obtain a steady-state solution for the particle size distribution is analysed. For the numerical simulation with a fluid Reynolds number of $Re_f = 22,500$, the dimensionless length to reach the steady-state solution is seen in Fig. 4. The steady-state solution for the particle size distribution is obtained after a dimensionless flow length of $\tilde{L} \approx 450$. It is therefore concluded that a periodic computational domain can be used to obtain steady-state solutions for the given geometry. The no-slip condition is applied to the walls of the domain for both phases.

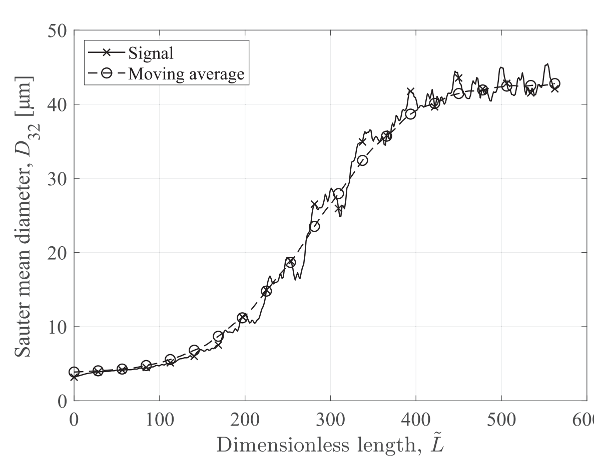

Fig. 4. Sauter mean diameter as a function of the dimensionless flow length, $\tilde{L}$ for $r_B = 1.5d_h, Re_f = 22,500, B = 50\cdot10^{-7}$ and $C_4 = 2$.

4.2. Mesh independence study

The number of computational cells in the domain is increased to a point where a solution that is independent of the number of computational cells is obtained. The parameter of interest in this study is the particle size distribution and the volume-averaged Sauter mean diameter which is seen in Fig. 5 for three different mesh sizes. The coarse mesh consists of 97,000 cells, the medium mesh consists of 313,000 cells and the fine mesh consists of 521,000 cells. The mesh is refined in the axial and radial direction, but keeping a constant minimum cell size at the wall. A mesh independent particle size distribution is obtained using the medium-sized mesh, which is also the computational mesh seen in Fig. 3.

4.3. Validation of model parameters

Two model properties are varied to find particle characteristics that resemble the experimental measurements. The particle critical strength parameter, B, and the daughter size distribution coefficient, C_4, is varied to see the effect of that given parameter and to find suitable properties for the particles.

4.3.1. Critical strength parameter

The particle strength parameter, B, is varied for a constant fluid Reynolds number, to analyse the effect on the particle size distribution when changing the critical strength. The fluid Reynolds number resembles that of the experimental measurements, $Re_{\mathrm{f}} = 22,500$, and the strength parameter was varied from $40 \cdot 10^{-7} < B < 60 \cdot 10^{-7}$. The daughter size distribution coefficient C_4 is set to $C_4 = 2$ for this parameter study. The steady-state particle size distribution at the outlet of the domain is seen in Fig. 6. The shape of the particle size distribution is similar for the three values of B, but the peak of the particle size distribution increases as B decreases. Using a strength parameter of $B = 50 \cdot 10^{-7}$ m^3/s^3 produces results that are in good agreement with the experimentally obtained particle size distribution. This value will be used for further analysis of the impact of the fluid Reynolds number and the effect of the pipe bend radius.

4.3.2. Daughter size distribution coefficient

For studying the impact of the daughter size distribution coefficient C_4, simulations are carried out using $C_4 = 2, C_4 = 4$ and $C_4 = 6$. The number of agglomerate fragments increases with the coefficient, meaning that smaller daughter particles are favoured. The particle size distribution for the different daughter distribution coefficients is seen in Fig. 7, where the experimentally measured particle size distribution is shown for reference. An increased concentration of smaller particles is observed when C_4 increases, as expected. It is seen that a daughter size distribution coefficient of $C_4 = 2$ produces a particle size distribution in good agreement with the experimental results, which corresponds to binary breakage according to Eq. (26).

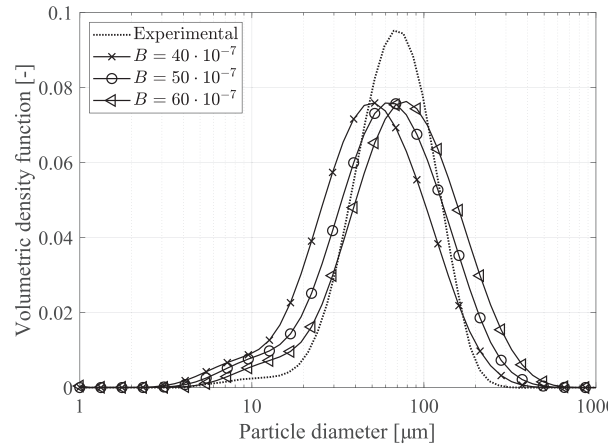

Fig. 6. Particle size distribution for strength parameters, B, compared to experimentally obtained particle size distribution using a Malvern Mastersizer 3000. Lowering the strength parameters results in an increased number of smaller particles.

4.4. Flow field

The normalised fluid velocity, $|\boldsymbol{u}_{\mathrm{f}}|/\bar{u}_{\mathrm{f}}$, is seen, as a contour in the middle of the pipe, in Fig. 8a for $Re_{\mathrm{f}} = 22,500$ and $r_{\mathrm{B}} = 1.5d_{\mathrm{h}}$. Larger absolute velocities are observed at the beginning of the pipe U-bend, as the fluid is forced towards the outer radius of the bend, due to the strong curvature which effectively causing a downstream separation zone. The separation zone is a function of the curvature of the bend and also of the velocity of the fluid, as the fluid is more prone to stay attached at lower velocities. The high-velocity zones are also the zones with the highest velocity gradients, as the fluid changes direction within the U-bends. Therefore, the U-bends are the zones where the particles are most prone to breakage, which is seen when analysing the contours of the particle number concentration and the Sauter mean diameter in Fig. 8b

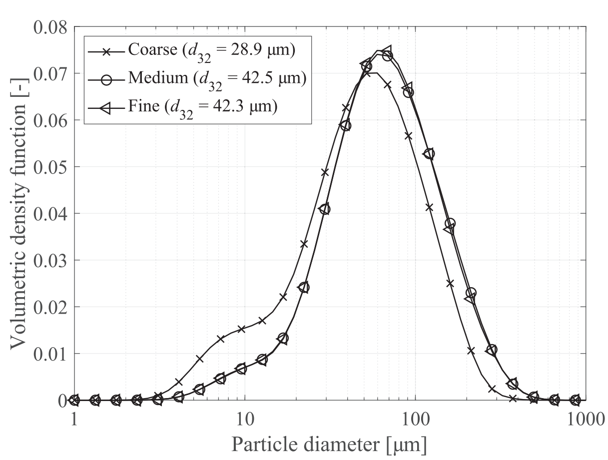

Fig. 5. Particle size distribution for three different computational mesh sizes with the parameters of $Re_{\mathrm{f}} = 22,500, r_{\mathrm{B}} = 1.5d_{\mathrm{h}}, B = 50 \cdot 10^{-7}$ and $C_4 = 2$.

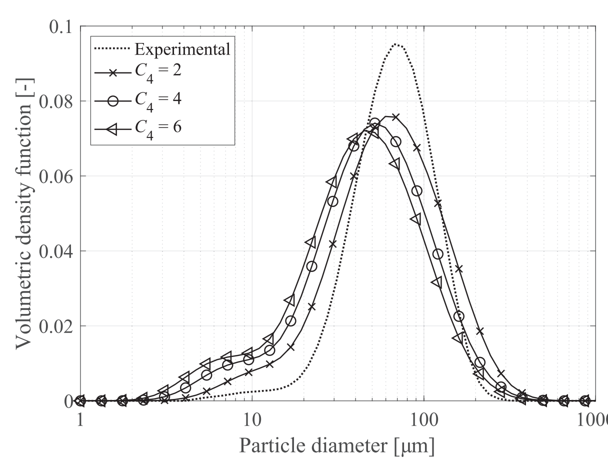

Fig. 7. Particle size distribution of $Re_{\mathrm{f}} = 22,500$ and $r_{\mathrm{B}} = 1.5d_{\mathrm{h}}$ for different daughter size distribution coefficients, C_4, with the experimentally obtained particle size distribution for reference.

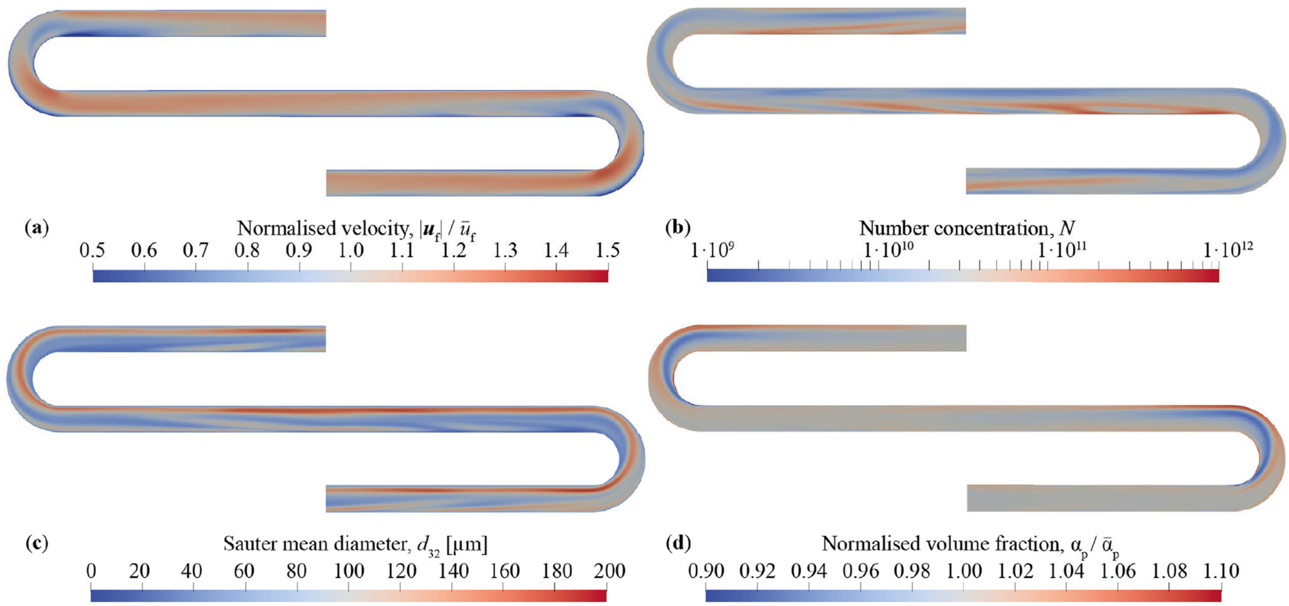

Fig. 8. Steady-state contour plots for the geometrical symmetry plane of the computational domain for $Re_f = 22,500$, $B = 50 \cdot 10^{-7}$ and $C_4 = 2$. (**a**): Normalised fluid velocity, $|\boldsymbol{u}_f|/\bar{u}_f$. (**b**): Number concentration of the particle phase. (**c**): Sauter mean diameter, d_{32}, of the particle phase. (**d**): Normalised volume fraction of the particle phase, $\alpha_f/\bar{\alpha}_f$.

and 8c, respectively. The high curvature of the bend forces the two phases to separate and a larger volume fraction is observed in the 180° bend, as seen when analysing the normalised volume fraction of the particle phase in Fig. 8d. The heavier particle phase is forced towards the circumference of the bend.

4.5. Variation of flow parameters

The fluid Reynolds number and the geometrical setup of the 180° bend are varied to study their effect on the particle size distribution. These parameters are chosen to analyse the effect of increasing the volumetric flow rate through the same static flocculator or changing the bend radius of the static flocculator in the design process.

4.5.1. Fluid Reynolds number

The fluid Reynolds number is varied in the range of $15,000 < Re_f < 35,000$ and the resulting steady-state particle size distributions are seen in Fig. 9. When the fluid Reynolds number increases, more turbulence is generated. This means that the turbulent energy dissipation rate increases overall in the computational domain and also at the 180° bends. As a result, breakage outweighs aggregation, thereby resulting in a distribution that is shifted towards smaller sizes.

It is observed how the mean particle diameter decreases along the inner circumference of the 180° bend when analysing the contour plot of the Sauter mean diameter in Fig. 8c. This is also where the turbulent energy dissipation rate is largest, which is causing the particles to break up. Downstream of the U-bend the mean particle diameter increases again as the turbulent dissipation rate decreases, resulting in an increased agglomeration.

4.5.2. Pipe bend radius

To analyse the impact of the geometrical setup, the bend radius of the pipe is varied. Three of the most common industrial bend radii are used: $r_B = d_h, r_B = 1.5d_h$ and $r_B = 2.5d_h$. The fluid Reynolds number is again varied within the range of $15,000 < Re_f < 35,000$ and the Sauter mean diameter is plotted as a function of the fluid Reynolds number in Fig. 10. It is seen that

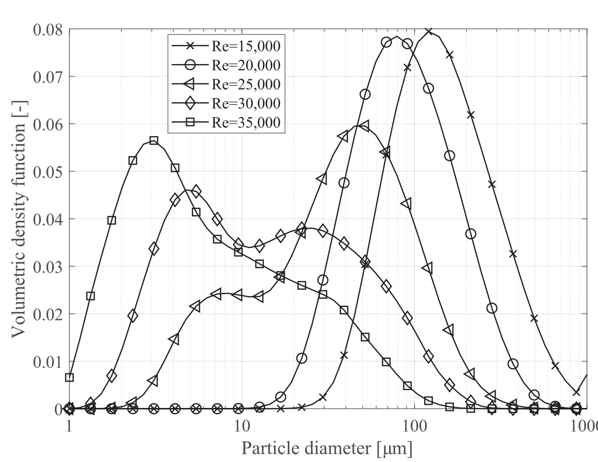

Fig. 9. Particle size distribution for different fluid Reynolds numbers for $r_B = 1.5d_h$.

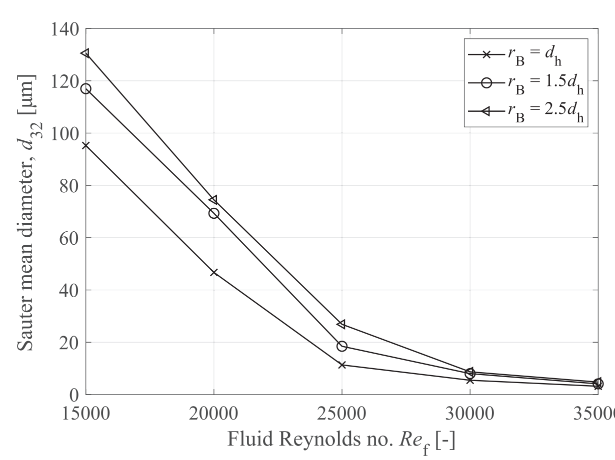

Fig. 10. Sauter mean diameter, d_{32}, as a function of the fluid Reynolds number for three different pipe bend radii.

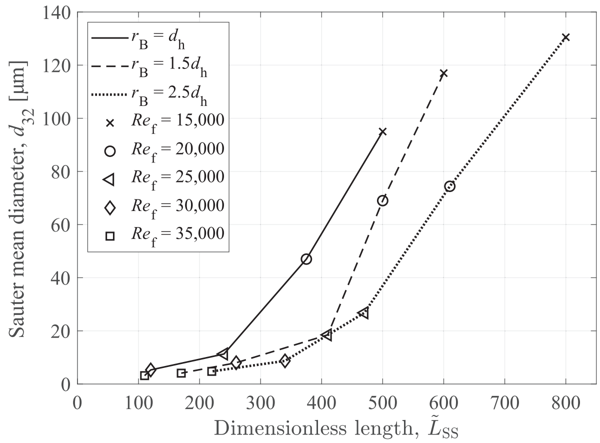

Fig. 11. Sauter mean diameter, d_{32}, as a function of the dimensionless length $\widetilde{L}_{SS}$ needed to obtain a steady-state solution for the different bend radii and fluid Reynolds numbers.

as the fluid Reynolds number increases, the particle Sauter mean diameter decreases and converges to a constant value for all pipe bend radii. This effect is due to more turbulence being induced in the fluid domain, thereby increasing the turbulent energy dissipation rate in the overall computational domain. It is therefore observed that the bend radius of the pipe has a negligible impact on the Sauter mean diameter of the particles if the fluid Reynolds number exceeds $Re_f > 30{,}000$, for the particle properties chosen.

When analysing the dimensionless length needed to obtain a steady-state solution, $\widetilde{L}_{SS}$, in Fig. 11, it is seen that the response length of the system increases with the bend radius of the pipe. It is also observed that the response length decreases when the fluid Reynolds number increases. The experimental setup, see Fig. 2, has a total dimensionless length of $\widetilde{L} = 500$, and therefore the largest particle size distribution that can be obtained within this length is given by choosing a bend radius of $r_B = d_h$ and a fluid Reynolds number of $Re_f = 15{,}000$. By choosing this configuration, the Sauter mean diameter increases from $d_{32} = 42.7\,\mu m$ to $d_{32} = 95\,\mu m$ without changing the dimensionless length of the experimental setup.

5. Conclusion

A numerical model for predicting the particle size distribution when accounting for particle agglomeration and breakage is presented in this study in conjunction with an experimentally obtained particle size distribution of flocculated soot particles. The fluid and particle phases are modelled using the multi-fluid model, where the particle number density function is tracked by solving the population balance equation with the method of classes. Special care is taken to account for the interfacial momentum transfer between the fluid and solid phase. Furthermore, agglomeration and breakage kernels are applied for the turbulent regime, to obtain a steady-state solution for the particle size distribution.

Several simulations are carried out to analyse and find suitable parameters that describe the agglomeration and breakage of soot-like particles in the Euler-Euler model. Using the critical turbulent energy dissipation rate and daughter size distribution, suitable numerical parameters are presented which obtain results in good agreement with the experimental data.

The particle size distribution for fluid Reynolds numbers in the range of $15{,}000 < Re_f < 35{,}000$ is analysed for three different pipe bend radii of $r_B = d_h, r_B = 1.5d_h$ and $r_B = 2.5d_h$. It is shown that the pipe bend radius has a negligible impact on the Sauter mean diameter when the fluid Reynolds number exceeds $Re_f > 30{,}000$ for the selected particle parameters. It has been shown that the Sauter mean diameter can be increased from $d_{32} = 42.7\,\mu m$ to $d_{32} = 95\,\mu m$ by decreasing the pipe bend radius from $r_B = 1.5d_h$ to $r_B = d_h$ and decreasing the fluid Reynolds number from $Re_f = 22{,}500$ to $Re_f = 15{,}000$ while maintaining a maximum flow length of $\tilde{L} = 500$.

6. Additional information

The implementation of the aggregation- and breakage kernels as well as the Saffman-Mei lift force models is published through the HZDR Multiphase Addon for OpenFOAM (Schlegel et al., 2022) and has also been contributed to the main OpenFOAM release (Foundation, 2022).

Declaration of Competing Interest

The authors declare that they have no known competing financial interests or personal relationships that could have appeared to influence the work reported in this paper.

Acknowledgements

This work is financially supported by Innovation Fund Denmark under Grant No. 9065-00188B. Special appreciation is given to Anders Schou Simonsen and Thomas Condra for their valuable inputs and comments during this work.

Nomenclature	
A	Area (m^2)
a	Aggregation frequency
B	Strength parameter (m^3/s^3)
b	Breakage frequency
C	Constant (-)
CFL	Courant–Friedrichs–Lewy number ($u\Delta t/\Delta x$)
d	Diameter (m)
D_f	Fractal dimension (-)
e	Coefficient of restitution (-)
F	Force (N)
G	Velocity gradient (1/s)
g	Gravitational acceleration (m/s^2)
k	Turbulent kinetic energy (m^2/s^2)
M	Interfacial momentum transfer
N	Number concentration
n	Number (-)
p	Pressure (Pa)
r	Radius (m)
Re	Reynolds number ($\lvert u\rvert d_h/\nu$)
S	Source term
t	Time (s)
u	Velocity (m/s)
v	Volume (m^3)
Greek letters	
α	Volume fraction (-)
β	Daughter size distribution function
ε	Turbulent energy dissipation rate (m^2/s^3)
μ	Dynamic viscosity (Pa s)
ν	Kinematic viscosity (m^2/s)
ρ	Density (kg/m^3)
σ	Turbulent Schmidt number (-)

(*continued on next page*)

τ	Stress tensor (N/m^2)
ω	Vorticity ($\nabla \times \boldsymbol{u}$)
Subscripts	
0	Primary particle
32	Sauter mean
φ	Phase
ω	Vorticity
B	Bend
c	Collision radius
cr	Critical rate
D	Drag
disp	Turbulent dispersion
f	Fluid
h	Hydraulic
L	Lift
p	Particle
r	Relative
VM	Virtual mass

Appendix A. Submodels applied for KTGF theory

Mathematical equations for the submodels applied for the kinetic theory of granular flow is presented in this appendix to support Table 1.

A.1. Radial distribution function

The mathematical expression for the radial distribution function, g_0, by Lun and Savage (1986) is given as

$$g_0 = \left(1 - \frac{\alpha_p}{\alpha_{p,max}}\right). \tag{A.1}$$

A.2. Conductivity of granular energy

The mathematical expression of Hrenya and Sinclair (1997) to account for conductivity of granular energy is given by

$$\kappa = \frac{25\sqrt{\pi\Theta}}{128}\rho_p d_p\left[\left(\frac{1}{1+\frac{\lambda_{mfp}}{R}}\frac{8}{\eta g_0} + \frac{96\alpha_p}{5}\right)\left(\frac{1+\frac{12}{5}\eta^2(4\eta-3)\alpha_p g_0}{41-33\eta}\right) + \frac{512}{25\pi}\eta\alpha_p^2 g_0\right], \tag{A.2}$$

where Θ is the granular energy, λ_{mfg} is the mean free path, e is the coefficient of restitution, $\eta = 1/2(1+e)$ and R is the characteristic length.

A.3. Frictional stress

The semi-empirical equation proposed by Johnson and Jackson (1987) for the normal frictional stress, P_f, is given as

$$P_f = \mathrm{Fr}\frac{(\alpha_p - \alpha_{p,min})^n}{(\alpha_{p,max} - \alpha_p)^p}, \tag{A.3}$$

where Fr, n and p are empirical material constants and $\alpha_p > \alpha_{p,min}$. The volume fraction at where frictionla stresses become significant is denoted by $\alpha_{p,min}$ and in this study this value chosen $\alpha_{p,min} = 0.01$, meaning frictional stresses are assumed negligible for dilute particle flow.

A.4. Generation and dissipation of granular energy

The mathematical expression for generation and dissipation of granular energy, λ_p, by Lun et al. (1984) is given as

$$\lambda_p = 12(1-e^2)\frac{\alpha_p\rho_p g_0}{d_p\sqrt{\pi}}\Theta^{3/2}. \tag{A.4}$$

A.5. Particle shear viscosity

The mathematical expression for particle shear viscosity, μ_p of Hrenya and Sinclair (1997) is given by

$$\mu_p = \frac{5\sqrt{\pi\Theta}}{96}\rho_p d_p\left[\left(\frac{1}{\eta g_0} + \frac{8\alpha_p}{5}\right)\left(\frac{1+\frac{8}{5}\eta(3\eta-2)\alpha_p g_0}{2-\eta}\right) + \frac{768}{25\pi}\eta\alpha_p^2 g_0\right]. \tag{A.5}$$

A.6. Particle phase pressure

The solid-phase pressure, P_p, represents the normal forces due to particle–particle collisions. The mathematical formulation of Lun et al. (1984) is given as

$$P_p = \rho_p\alpha_p\Theta[1 + 2(1+e)g_0\alpha_p]. \tag{A.6}$$

References

Adachi, Y., Cohen Stuart, M.A., Fokkink, R., 1994. Kinetics of Turbulent Coagulation Studied by Means of End-over-End Rotation. J. Colloid Interface Sci. 165, 310–317. https://doi.org/10.1006/JCIS.1994.1234.

Bhandari, J., China, S., Chandrakar, K.K., Kinney, G., Cantrell, W., Shaw, R.A., Mazzoleni, L.R., Girotto, G., Sharma, N., Gorkowski, K., Gilardoni, S., Decesari, S., Facchini, M.C., Zanca, N., Pavese, G., Esposito, F., Dubey, M.K., Aiken, A.C., Chakrabarty, R.K., Moosmüller, H., Onasch, T.B., Zaveri, R.A., Scarnato, B.V., Fialho, P., Mazzoleni, C., 2019. Extensive Soot Compaction by Cloud Processing from Laboratory and Field Observations. Scientific Reports 2019 9:1 9, 1–12. doi:10.1038/s41598-019-48143-y.

Bratby, J., 2006. Coagulation and flocculation in water and wastewater treatment. AUG., IWA Publishing. https://doi.org/10.2166/9781780407500.

Bridgeman, J., Jefferson, B., Parsons, S.A., 2010. The development and application of CFD models for water treatment flocculators. Adv. Eng. Softw. 41, 99–109. https://doi.org/10.1016/J.ADVENGSOFT.2008.12.007.

Burns, A.D., Frank, T., Hamill, I., Shi, J.M., 2004. The Favre averaged drag model for turbulent dispersion in Eulerian multi-phase flows. In: 5th International Conference on Multiphase Flow, pp. 1–17.

Cai, L., Liu, Z., Mi, S., Luo, C., Ma, K., Xu, A., Yang, S., 2019. Investigation on flow characteristics of ice slurry in horizontal 90° elbow pipe by a CFD-PBM coupled model. Adv. Powder Technol. J. 30, 2299–2310. https://doi.org/10.1016/j.apt.2019.07.010.

Camp, T.R., Stein, P.C., 1943. Velocity Gradients and Internal Work in Fluid Motion. J. Boston Soc. Civil Eng. 30, 219–237.

David Griffith, J., Williams, R.G., 1972. Application of Jar-Test Analysis at Phoenix. Ariz. J. (Am. Water Works Assoc.) 64, 825–830.

Dizaji, F.F., Marshall, J.S., Grant, J.R., 2019. Collision and breakup of fractal particle agglomerates in a shear flow. J. Fluid Mech. 862, 592–623. https://doi.org/10.1017/jfm.2018.959.

Ducoste, J.J., Clark, M.M., 1999. Turbulence in flocculators: Comparison of measurements and CFD simulations. AIChE J. 45, 432–436. https://doi.org/10.1002/aic.690450222.

Escue, A., Cui, J., 2010. Comparison of turbulence models in simulating swirling pipe flows. Appl. Math. Model. 34, 2840–2849. https://doi.org/10.1016/J.APM.2009.12.018.

Ganesan, S., 2012. An operator-splitting Galerkin/SUPG finite element method for population balance equations: stability and convergence. ESAIM. Math. Model. Numer. Anal. 46, 1447–1465. https://doi.org/10.1051/M2AN/2012012.

Haarhoff, J., van der Walt, J.J., 2001. Towards optimal design parameters for around-the-end hydraulic flocculators. J. Water Supply: Res. Technol.-Aqua 50, 149–160. https://doi.org/10.2166/aqua.2001.0014.

Hærvig, J., Sørensen, K., Condra, T.J., 2018. Early stages of agglomeration of adhesive particles in fully-developed turbulent pipe flows. Int. J. Multiph. Flow 106, 254–267. https://doi.org/10.1016/J.IJMULTIPHASEFLOW.2018.04.017.

Hilgenstock, A., Ernst, R., 1996. Analysis of installation effects by means of computational fluid dynamics—CFD vs experiments? Flow Meas. Instrum. 7, 161–171. https://doi.org/10.1016/S0955-5986(97)88066-1.

Hrenya, C.M., Sinclair, J.L., 1997. Effects of particle-phase turbulence in gas-solid flows. AIChE J. 43, 853–869. https://doi.org/10.1002/AIC.690430402.

Jeldres, R.I., Fawell, P.D., Florio, B.J., 2017. Population balance modelling to describe the particle aggregation process: A review. Powder Technol. 326, 190–207. https://doi.org/10.1016/j.powtec.2017.12.033.

Johnson, K.L., Kendall, K., Roberts, A.D., 1971. Surface energy and the contact of elastic solids. Proc. R. Soc. Lond. Ser. A 324, 301–313. https://doi.org/10.1098/rspa.1971.0141.

Johnson, P.C., Jackson, R., 1987. Frictional–collisional constitutive relations for granular materials, with application to plane shearing. J. Fluid Mech. 176, 67–93. https://doi.org/10.1017/S0022112087000570.
Kim, J., Yadav, M., Kim, S., 2014. Characteristics of Secondary Flow Induced by 90-Degree Elbow in Turbulent Pipe Flow. Engineering Applications of Computational Fluid Mechanics 8, 229–239. https://doi.org/10.1080/19942060.2014.11015509.
Kumar, S., Ramkrishna, D., 1996. On the solution of population balance equations by discretization—I. A fixed pivot technique. Chem. Eng. Sci. 51, 1311–1332. https://doi.org/10.1016/0009-2509(96)88489-2.
Kusters, K.A., 1991. The influence of turbulence on aggregation of small particles in agitated vessels Ph.D. thesis. Technische Universiteit Eindhoven. https://doi.org/10.6100/IR362582.
Laakkonen, M., Moilanen, P., Alopaeus, V., Aittamaa, J., 2007. Modelling local bubble size distributions in agitated vessels. Chem. Eng. Sci. 62, 721–740. https://doi.org/10.1016/J.CES.2006.10.006.
Lee, C.S., Robinson, J., Chong, M.F., 2014. A review on application of flocculants in wastewater treatment. Process Saf. Environ. Prot. 92, 489–508. https://doi.org/10.1016/J.PSEP.2014.04.010.
Lehnigk, R., Bainbridge, W., Liao, Y., Lucas, D., Niemi, T., Peltola, J., Schlegel, F., 2021. An open-source population balance modeling framework for the simulation of polydisperse multiphase flows. AIChE J., e17539 https://doi.org/10.1002/AIC.17539.
Li, D., Gao, Z., Buffo, A., Podgorska, W., Marchisio, D.L., 2017. Droplet breakage and coalescence in liquid–liquid dispersions: Comparison of different kernels with EQMOM and QMOM. AIChE J. 63, 2293–2311. https://doi.org/10.1002/AIC.15557.
Liu, J., Crapper, M., McConnachie, G., 2004. An accurate approach to the design of channel hydraulic flocculators. Water Res. 38, 875–886. https://doi.org/10.1016/J.WATRES.2003.10.014.
Lun, C.K.K., Savage, S.B., 1986. The effects of an impact velocity dependent coefficient of restitution on stresses developed by sheared granular materials. Acta Mechanica 1986 63:1 63, 15–44. doi:10.1007/BF01182538.
Lun, C.K.K., Savage, S.B., Jeffrey, D.J., Chepurniy, N., 1984. Kinetic theories for granular flow: inelastic particles in Couette flow and slightly inelastic particles in a general flowfield. J. Fluid Mech. 140, 223–256. https://doi.org/10.1017/S0022112084000586.
Ma, X., Zangmeister, C.D., Gigault, J., Mulholland, G.W., Zachariah, M.R., 2013. Soot aggregate restructuring during water processing. J. Aerosol Sci. 66, 209–219. https://doi.org/10.1016/j.jaerosci.2013.08.001.
Mandelbrot, B.B., 1985. Self-Affine Fractals and Fractal Dimension. Phys. Scr. 32, 257. https://doi.org/10.1088/0031-8949/32/4/001.
Marchisio, D.L., Vigil, R.D., Fox, R.O., 2003. Implementation of the quadrature method of moments in CFD codes for aggregation - breakage problems. Chem. Eng. Sci. 58, 3337–3351. https://doi.org/10.1016/S0009-2509(03)00211-2.
Marshall, E.M., Bakker, A., 2004. Computational Fluid Mixing. Handbook of industrial mixing: science and practice, 257–343.
Mei, R., 1992. An approximate expression for the shear lift force on a spherical particle at finite reynolds number. Int. J. Multiph. Flow 18, 145–147. https://doi.org/10.1016/0301-9322(92)90012-6.
Mhaisalkar, V.A., Paramasivam, R., Bhole, A.G., 1991. Optimizing physical parameters of rapid mix design for coagulation-flocculation of turbid waters. Water Res. 25, 43–52. https://doi.org/10.1016/0043-1354(91)90097-A.
Mikhailov, E.F., Vlasenko, S.S., Podgorny, I.A., Ramanathan, V., Corrigan, C.E., 2006. Optical properties of soot–water drop agglomerates: An experimental study. Journal of Geophysical Research: Atmospheres 111, 7209. https://doi.org/10.1029/2005JD006389.
Nan, J., Yao, M., Chen, T., Wang, Z., Li, Q., Zhan, D., 2016. Experimental and numerical characterization of floc morphology: role of changing hydraulic retention time under flocculation mechanisms. Environ. Sci. Pollut. Res. 23, 3596–3608. https://doi.org/10.1007/s11356-015-5539-7.
Palzer, S., 2011. Agglomeration of pharmaceutical, detergent, chemical and food powders — Similarities and differences of materials and processes. Powder Technol. 206, 2–17. https://doi.org/10.1016/J.POWTEC.2010.05.006.
Passalacqua, A., Laurent, F., Madadi-Kandjani, E., Heylmun, J.C., Fox, R.O., 2018. An open-source quadrature-based population balance solver for OpenFOAM. Chem. Eng. Sci. 176, 306–318. https://doi.org/10.1016/J.CES.2017.10.043.
Saffman, P., 1965. The lift on a small sphere in a slow shear flow. Journal of Fluid Mechanics1 22, 385–400. https://doi.org/10.1017/S0022112065000824.
Schlegel, F., Bilde, K.G., Draw, M., Evdokimov, I., Hänsch, S., Khan, H., Lehnigk, R., Li, J., Lyu, H., Meller, R., Petelin, G., Tekavčič, M., 2022. HZDR Multiphase Addon for OpenFOAM. https://doi.org/10.14278/RODARE.767.
Shekhawat, L.K., Sarkar, J., Gupta, R., Hadpe, S., Rathore, A.S., 2018. Application of CFD in Bioprocessing: Separation of mammalian cells using disc stack centrifuge during production of biotherapeutics. J. Biotechnol. 267, 1–11. https://doi.org/10.1016/J.JBIOTEC.2017.12.016.
Simonsen, A.S., 2018. Modelling and Analysis of Seawater Scrubbers for Reducing SOx Emissions from Marine Engines. Technical Report. Aalborg University. Aalborg.
The OpenFOAM Foundation, 2022. OpenFOAM-dev.
Tong, Z., Zhong, W., Yu, A., Chan, H.K., Yang, R., 2016. CFD–DEM investigation of the effect of agglomerate–agglomerate collision on dry powder aerosolisation. J. Aerosol Sci. 92, 109–121. https://doi.org/10.1016/J.JAEROSCI.2015.11.005.
Trivanovic, U., Corbin, J.C., Baldelli, A., Peng, W., Yang, J., Kirchen, P., Miller, J.W., Lobo, P., Gagné, S., Rogak, S.N., 2019. Size and morphology of soot produced by a dual-fuel marine engine. Journal of Aerosol Science journal 138, 105448. https://doi.org/10.1016/j.jaerosci.2019.105448.
Vrale, L., Jorden, R.M., 1971. Rapid Mixing in Water Treatment. J. (Am. Water Works Assoc.) 63, 52–58.
van Wachem, B., 2000. Derivation, Implementation, and Validation of Computer Simulation Models for Gas-Solid Fluidized Beds.
Wang, X., Wang, Y., Bai, Y., Wang, P., Zhao, Y., 2018. An overview of physical and chemical features of diesel exhaust particles. https://doi.org/10.1016/j.joei.2018.11.006.
Wang, Z., Nan, J., Ji, X., Yang, Y., 2018. Effect of the micro-flocculation stage on the flocculation/sedimentation process: The role of shear rate. Sci. Total Environ. 633, 1183–1191. https://doi.org/10.1016/J.SCITOTENV.2018.03.286.
Wen, C., Yu, Y., 1966. Mechanics of Fluidization. Chem. Eng. Prog. Symp. Ser. 162, 100–111.
Yakhot, V., Orszag, S.A., 1986. Renormalization group analysis of turbulence. I. Basic theory. Journal of Scientific Computing 1986 1:1 1, 3–51. doi:10.1007/BF01061452.
Yakhot, V., Orszag, S.A., Thangam, S., Gatski, T.B., Speziale, C.G., 1992. Development of turbulence models for shear flows by a double expansion technique. Phys. Fluids A 4, 1510–1520. https://doi.org/10.1063/1.858424.
Yao, Y., Su, J.W.W., Luo, Z.H.H., 2015. CFD-PBM modeling polydisperse polymerization FBRs with simultaneous particle growth and aggregation: The effect of the method of moments. Powder Technol. 272, 142–152. https://doi.org/10.1016/j.powtec.2014.11.037.
Yuan, C., Laurent, F., Fox, R.O., 2012. An extended quadrature method of moments for population balance equations. J. Aerosol Sci. 51, 1–23. https://doi.org/10.1016/J.JAEROSCI.2012.04.003.
Zhu, Z., Dorao, C.A., Lucas, D., Jakobsen, H.A., 2009. On the Coupled Solution of a Combined Population Balance Model Using the Least-Squares Spectral Element Method. Ind. Eng. Chem. Res. 48, 7994–8006. https://doi.org/10.1021/IE900088Q.